

Engineering spatial coherence in lattices of polariton condensates: supplement

J. D. TÖPFER,^{1,2}  I. CHATZOPOULOS,¹ H. SIGURDSSON,^{1,2}  T. COOKSON,¹ Y. G. RUBO,³  AND P. G. LAGOUDAKIS^{1,2,*}

¹*School of Physics and Astronomy, University of Southampton, Southampton, SO17 1BJ, UK*

²*Skolkovo Institute of Science and Technology, Moscow, Bolshoy Boulevard 30, bld. 1, 121205, Russia*

³*Instituto de Energías Renovables, Universidad Nacional Autónoma de México, Temixco, Morelos, 62580, Mexico*

*Corresponding author: P.Lagoudakis@skoltech.ru

This supplement published with The Optical Society on 19 January 2021 by The Authors under the terms of the [Creative Commons Attribution 4.0 License](https://creativecommons.org/licenses/by/4.0/) in the format provided by the authors and unedited. Further distribution of this work must maintain attribution to the author(s) and the published article's title, journal citation, and DOI.

Supplement DOI: <https://doi.org/10.6084/m9.figshare.13344902>

Parent Article DOI: <https://doi.org/10.1364/OPTICA.409976>

Engineering spatial coherence in lattices of polariton condensates: supplemental document

1. METHODS

A. Experimental methods

We utilise a strain-compensated 2λ GaAs microcavity with embedded InGaAs quantum wells and a quality factor $Q \approx 12\,000$ [1]. We continuously cool the microcavity sample in a cold-finger cryostat ($T \approx 6$ K) and operate at a negative cavity-detuning of $\Delta \approx -5$ meV resulting in a lower polariton mode at $\lambda \approx 858$ nm for zero in-plane momentum $|\mathbf{k}| = 0$. We use a circularly polarised non-resonant blue-detuned ($\lambda \approx 800$ nm) pulsed laser (pulse duration ≈ 150 fs, repetition rate 80 MHz). For each condensate node the laser is focused onto the microcavity sample to a beam waist of approximately $2\ \mu\text{m}$ via a 0.4 NA microscope objective. Polariton photoluminescence (PL) and the excitation laser are measured by imaging the cavity emission or reflected light of the microcavity sample onto a CCD sensor with integration times in the range of 10-100 ms, which corresponds to averaging measurements over approximately one million realisations of the system. By using a longpass or shortpass filter in front of the camera we can selectively choose to measure either the spatial geometry of the polariton emission or the excitation laser.

Experimental details of the density stabilisation technique for polariton condensate lattices are given in Supplementary Section 3. Methods for the measurement of the mutual complex coherence factor μ_{ij} between any pair of condensate nodes are described in Supplementary Sections 4 and 5.

B. Numerical Simulations

A stochastic dissipative Gross-Pitaevskii equation describes the polariton condensate order parameter $\Psi(\mathbf{r}, t)$ coupled to a rate equation describing the density of a background excitonic reservoir n_x feeding particles into the condensate. The reservoir itself is sustained by a decaying population of excited electron-hole pairs $n_c(\mathbf{r}, t)$ which we assume are generated instantaneously by the sub-picosecond nonresonant Gaussian shaped pump $P(\mathbf{r})$,

$$i \frac{\partial \Psi}{\partial t} = \frac{1}{2} \left[-\frac{\hbar \nabla^2}{m} + V + \alpha |\Psi|^2 + i(Rn_x - \gamma) \right] \Psi + \frac{dW}{dt}, \quad (\text{S1a})$$

$$\frac{\partial n_x}{\partial t} = -(\Gamma_R + R|\Psi|^2) n_x + \mathcal{W} n_c, \quad (\text{S1b})$$

$$n_c = P(\mathbf{r}) e^{-(\mathcal{W} + \Gamma_c)t}. \quad (\text{S1c})$$

Here, m is the effective mass of a polariton in the lower dispersion branch, α is the interaction strength of two polaritons in the condensate, R is the rate of stimulated scattering of polaritons into the condensate from the active reservoir, γ is the polariton condensate decay rate, $\Gamma_{R,c}$ are the decay rates of the reservoir

excitons and electron-hole pairs respectively, \mathcal{W} is the conversion rate between the reservoir excitons and electron hole-pairs, and $V(\mathbf{r}, t) = g(n_x(\mathbf{r}, t) + n_c(\mathbf{r}, t))$ is the pump-induced potential with an effective reservoir-condensate interaction strength g . Here we have introduced a Gaussian white noise term dW based on a Monte Carlo technique in the truncated Wigner representation [2]. The correlators are written $\langle dW(\mathbf{r}_i) dW(\mathbf{r}_j) \rangle = 0$ and $\langle dW^*(\mathbf{r}_i) dW(\mathbf{r}_j) \rangle = (\Gamma + Rn_x) \delta(\mathbf{r}_i - \mathbf{r}_j) dt / 2\Delta A$ where ΔA is the cell area of the spatial grid. In analogy to our experiments, the integrated complex coherence factor $\tilde{\mu}_{ij}$ between two condensate nodes i and j [see Eq. (1) in the main text] is then calculated by averaging over multiple realisations of condensate formation. Good agreement between simulation and experimental data is obtained by only adjusting the values of g and $\max[P(\mathbf{r})]$ between different systems. The reason g is taken as a tuneable parameter is due to the fact that V can possess a more complicated sublinear dependence in Equation (S1a) as pointed out previously [3]. Parameters were set to: $\Gamma = 1/5.5\ \text{ps}^{-1}$, $\Gamma_R = 2\Gamma$, $\Gamma_c = 0.0055\Gamma$, $\mathcal{W} = 0.275\Gamma$, $\alpha = 0.01\ \text{ps}^{-1}\ \mu\text{m}^2$, $R = 0.05\alpha$, $m = 0.32\ \text{meV}\ \text{ps}^2\ \mu\text{m}^{-2}$, and $g = \{0.0008, 0.0011, 0.0022, 0.0016\}\alpha$ for dyad, chain, square, and triangle respectively.

2. COHERENCE IN POLARITON LATTICES

In our study of synchronisation in networks of coupled polariton condensates we are interested in the correlations between pairs of condensates which are described by their mutual coherence function

$$\Gamma_{ij}(t) = \langle \psi_i(t)^* \psi_j(t) \rangle,$$

where the brackets denote ensemble averaging and $\psi_i(t)$ is the complex-valued amplitude of the i th condensate node. The expectation value of the condensate's particle number (occupation) is given by the diagonal elements $\Gamma_{ii}(t)$, and the presence of non-zero off-diagonal elements $|\Gamma_{ij}(t)| > 0$ for $i \neq j$ indicates long-range order in the coupled condensate network. For nonstationary systems (such as for polariton condensates generated under pulsed excitation) the coherence function $\Gamma_{ij}(t)$ depends on time t . We note that pulsed excitation (≈ 150 fs pulse width) of ballistically coupled condensate nodes leads to polariton photoluminescence with typical emission signal full-width-at-half-maximum (FWHM) of 18 ps (see Supplementary Section 8). A normalised form of the mutual coherence function is given by the complex coherence factor

$$\mu_{ij}(t) = \frac{\Gamma_{ij}(t)}{\sqrt{\Gamma_{ii}(t)\Gamma_{jj}(t)}},$$

where for a fully coherent pair of condensates $|\mu_{ij}| = 1$. Considering measurements with time integration over many pulses we define the integrated complex coherence factor

$$\tilde{\mu}_{ij} = \frac{\int \Gamma_{ij}(t) dt}{\sqrt{\int \Gamma_{ii}(t) dt \int \Gamma_{jj}(t) dt}},$$

as an averaged measure for the mutual coherence properties of condensates in polariton networks. Throughout this manuscript time-integrated variables are marked with the tilde diacritic. For stationary ergodic systems (such as polariton condensates under constant pumping) the complex coherence factor $\mu_{ij}(t)$ does not depend on time and time-integrated measurements of correlations fully determine the coherence properties, i.e. $\mu_{ij}(t) = \tilde{\mu}_{ij}$. In case of pulsed excitation of polariton condensates the modulus of the time-integrated factor $|\tilde{\mu}_{ij}|$ represents a lower bound for the maximum value of the complex coherence factor $|\mu_{ij}(t)|$. We note that the argument of the integrated complex coherence factor represents the average condensate node phase difference $\tilde{\theta}_{ij} = \arg(\tilde{\mu}_{ij})$ and the integrated particle number $\int \Gamma_{ii}(t) dt$ of each condensate node is proportional to its measurable average emission intensity \tilde{I}_i .

3. FEEDBACK SCHEME

In this manuscript we present networks of ballistically coupled polariton condensates for which the pumping geometry has been adjusted using a reflective SLM (see Figure 1 in the main text) such as to equalise the emission power of each condensate node at condensation threshold. The algorithm used to calculate the holograms which are applied to the SLM is a modified version of the Gerchberg-Saxton (GS) algorithm [4] and takes into account feedback from the recorded PL in each iteration cycle. This iterative algorithm is similar to the schemes presented in Refs. [5, 6] applied to trapping of cold atoms. In our case the recorded PL of the condensates is not directly proportional to the pump power of each node but depends on the coupling-topology of the network, i.e. ballistic coupling between spatially separated condensate nodes affects the gain of each condensate.

The algorithm is schematically illustrated in Figure S1(a) and begins with the initialisation of a 2D complex field of amplitude $A^{(0)}(\mathbf{r})$ and phase $\phi^{(0)}(x, y)$ representing the amplitude of the pump laser and the phase hologram in pixel coordinates of the SLM, respectively. As an initial guess we assume a constant phase pattern $\phi^{(0)} = 0$ and a Gaussian field amplitude, whose width matches the pump laser width. In each iteration step n propagation of the complex field $A^{(0)} e^{i\phi^{(n)}(\mathbf{r})}$ from the SLM plane (source) to the focal plane (target) is computed by a fast Fourier transform (FFT) yielding a complex-valued target field with amplitude $\hat{A}^{(n)}(\mathbf{r})$ and phase $\hat{\phi}^{(n)}(\mathbf{r})$. Here, we use the hat symbol ($\hat{\cdot}$) to denote quantities in the target plane.

We add the output phase pattern $\phi^{(n)}$ with a device dependent correction term ϕ_c , which can also take into account optical aberrations in the experimental setup, and a blazed grating ϕ_g to offset the modulated laser beam from its unmodulated reflected part. The sum of these terms modulo the 2π bitlevel is applied to the SLM and defines the pump laser geometry in our experiment. In a next step we record the near-field photoluminescence of the polariton system excited by the current pump laser geometry and

extract the emission power $I_C^{(n)}$ of each condensate by integrating the recorded signal within the FWHM ($\approx 2 \mu\text{m}$) of each node. We update the target power $I_T^{(n+1)}$ for the next iteration step of the algorithm for each condensate node utilising the non-linear function

$$I_T^{(n+1)} = \frac{I_T^{(n)}}{1 + \epsilon \left(I_C^{(n)} / \langle I_C^{(n)} \rangle - 1 \right)}, \quad (\text{S2})$$

where ϵ is an adjustable feedback parameter and $\langle I_C^{(n)} \rangle$ denotes the mean of the measured condensate node emission distribution. The non-linear mapping given by Equation (S2) lowers (raises) the target pump power $I_T^{(n+1)}$ of nodes with measured emission power $I_C^{(n)}$ larger (lower) than the mean value $\langle I_C^{(n)} \rangle$. The parameter ϵ controls the speed of the feedback loop but cannot be set too large to avoid destabilisation of the algorithm. For $\epsilon = 0$ the algorithm depicted in Fig. S1(a) represents the conventional form of the GS algorithm with no iterative adjustment of target spot intensities, i.e. $I_T^{(n+1)} = I_T^{(n)}$, and the initial target pattern $I_T^{(0)}$ fully determines the outcome of the iterative Fourier transform algorithm.

Next, we calculate the two-dimensional field amplitude $\sqrt{\hat{I}_T^{(n+1)}}(\mathbf{r})$ which consists of the superposition of Gaussian spots representing the position and pump power of each condensate node in the target plane. The amplitude of each Gaussian peak is given by the square root of the updated spot power, i.e. $\sqrt{\hat{I}_T^{(n+1)}}$ and the width is related to the width of the Gaussian profile of the pump laser by means of a Fourier transform. The updated field amplitude feeds back into the GS cycle, where a complex-valued field with amplitude $\sqrt{\hat{I}_T^{(n+1)}}(\mathbf{r})$ and phase $\hat{\phi}^{(n)}(\mathbf{r})$ is constructed. Back-propagation of this complex field to the SLM plane is computed by an inverse fast Fourier transform (IFFT) yielding a phase pattern $\phi^{(n+1)}$ which replaces the initial phase pattern for the next iteration step, i.e. $\phi^{(n+1)} \rightarrow \phi^{(n)}$. The amplitude field at the SLM plane is kept constant as the initial field $A^{(0)}$ for each iteration step. We quit execution of the algorithm once the measured spot power distribution $I_C^{(n)}$ shows a spread which is smaller than a certain threshold level (usually 1% (RSD) reached within $\lesssim 100$ iterations).

We find good results for stabilising the intensity distribution in ballistically coupled polariton networks ($\text{RMS} \leq 1\%$) pumped at condensation threshold $P \gtrsim P_{\text{thr}}$ by choosing ϵ to be in the range $10^{-2} - 10^{-1}$. Stabilisation at larger pump powers $P \gg P_{\text{thr}}$ is impeded by the presented technique - which operates at a typical rate of 60 Hz - because of stronger nonlinear effects resulting in unstable regimes [7-9] and/or excitation of polaritons to higher energy states [10], with subsequent nonstationary condensate dynamics on a picosecond timescale.

In Figure S1(b) we show the recorded laser (pump) profile for a triangular lattice of 61 nodes (lattice constant $a = 14.9 \mu\text{m}$) using a phase hologram computed with the conventional GS algorithm ($\epsilon = 0$; 100 iterations). Although the target image is a laser pattern with homogeneous spot intensities, due to limited accuracy of the algorithm as well as unavoidable optical aberrations due to misalignment and device imperfections, the resultant experimentally obtained pump spot intensity distribution deviates from the

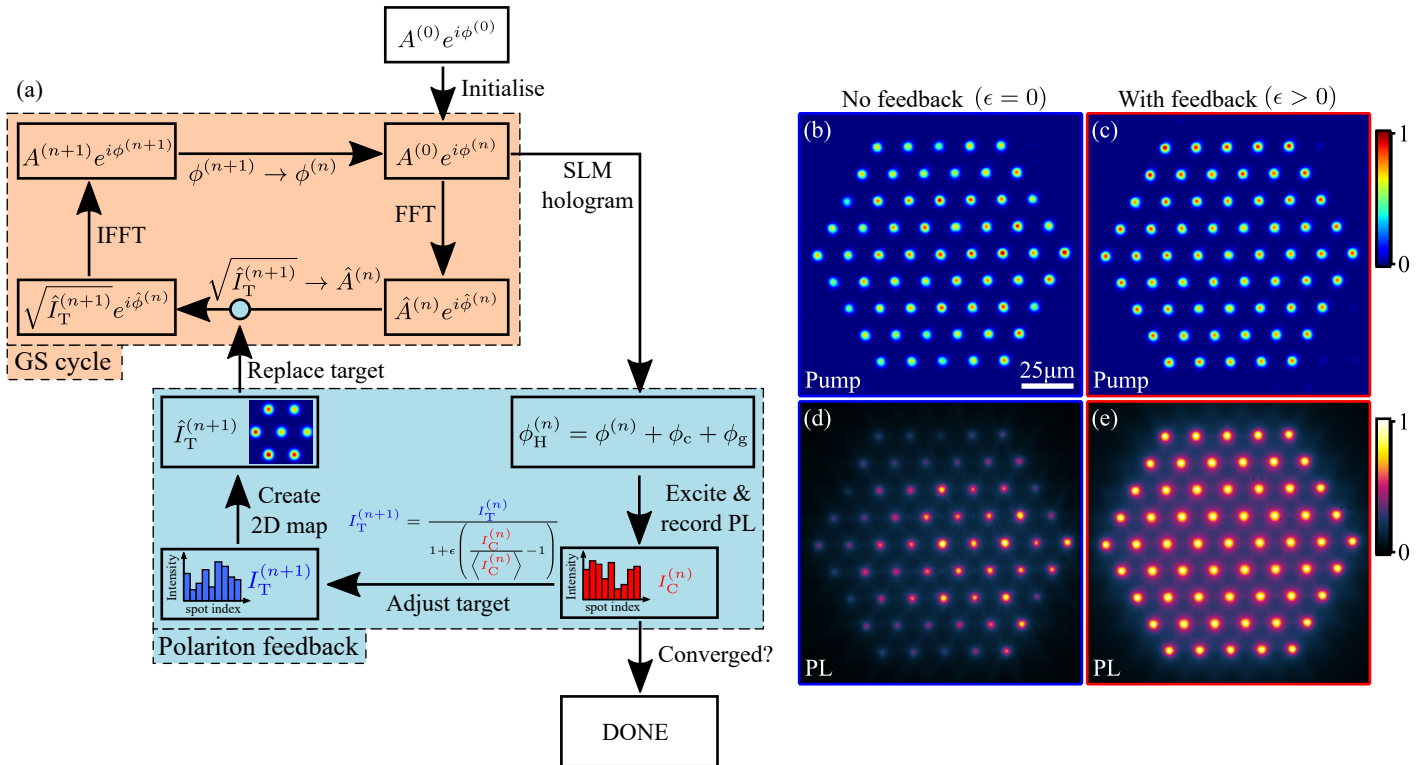


Fig. S1. (a) Schematic of the modified iterative Gerchberg-Saxton algorithm including feedback of the polariton photoluminescence (PL) to stabilise the node density in networks of coupled polariton condensates. (b,c) Recorded laser pump profile and (d,e) real space PL at condensation threshold without and with feedback, respectively.

homogeneous target. We measure a spread of $\approx 17\%$ (RSD) for the distribution of pump spot powers. Using the same pump profile to excite a triangular lattice of polariton condensates at condensation threshold ($P \approx P_{\text{thr}}$) we record the near-field PL as shown in Figure S1(d) and find an increased spread of condensate node densities of $\approx 37\%$ (RSD). While sample disorder can have an impact on the spatially dependent condensation threshold pump power and emission intensity for each condensate node, the main reason for the increased spread in the condensate emission power distribution is due to the system's nonlinear input-output-power characteristics and the finite size of the system. Nodes that are positioned at the edge of the condensate network are coupled to fewer nearest-neighbours (NN) than nodes in the bulk. Since coherent coupling between ballistically expanding polariton condensates results in a reduced condensation threshold [11], nodes coupled to fewer NNs will typically have a higher threshold pump power than nodes with a greater number of NNs (see Section 2B in the main text). As a result, condensate nodes in the bulk of the network generally have a larger occupation number (emission) than condensation nodes at the edges when pumped with the same excitation pump power [12]. This is a consequence of polariton waves radiating to the outside continuum and escaping the network which can be regarded as an effective flux-induced potential [13].

In Figs. S1(c,e) we show the recorded pump laser and corresponding near-field polariton emission profiles at threshold $P \approx P_{\text{thr}}$ after applying the intensity stabilisation feedback loop and termi-

nating it with spread in condensate node densities of $\approx 1\%$ (RSD). Comparison of the density spread and the spatial coherence in both polariton lattices without ($\epsilon = 0$) and with ($\epsilon > 0$) is shown in Figure 1 in the main text.

4. FARFIELD INTERFERENCE OF POLARITON LATTICES

The time-averaged far-field interference pattern $\bar{I}(\mathbf{k})$ of a set of N partially coherent, narrow-bandwidth and point-like light sources positioned in one plane can be written in the basis of spatial frequencies \mathbf{k} as (see Supplementary Section 11)

$$\bar{I}(\mathbf{k}) \propto \sum_{i,j=1}^N \sqrt{\bar{I}_i \bar{I}_j} \bar{\mu}_{ij} e^{i\mathbf{k} \cdot \mathbf{d}_{ij}}. \quad (\text{S3})$$

For each pair $\{i, j\}$ of point sources \mathbf{d}_{ij} denotes their in-plane spatial separation vector and $\bar{\mu}_{ij}$ their respective integrated complex coherence factor. For an incoherent system ($\bar{\mu}_{ij} = 0$ for $i \neq j$) the resulting homogeneous far-field radiation pattern is the incoherent superposition of light sources with individual intensities \bar{I}_i . However, for non-vanishing off-diagonal coherence elements ($|\bar{\mu}_{ij}| > 0$) the radiation pattern $\bar{I}(\mathbf{k})$ described in Equation (S3) becomes inhomogeneous and is formed by the sum over discrete Fourier-components $\exp(i\mathbf{k} \cdot \mathbf{d}_{ij})$ weighted by the integrated complex coherence factor $\bar{\mu}_{ij}$.

Hence, in analogy to beam interference measurements of coupled laser arrays [14], we can investigate the far-field emission

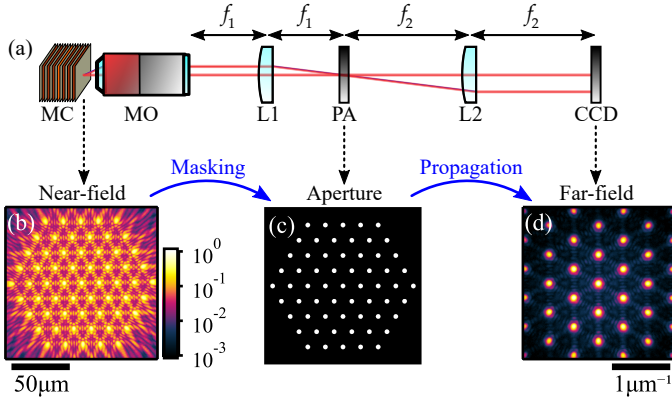


Fig. S2. Farfield interference of coherently coupled condensates. (a) Schematic of the experimental detection setup with microcavity (MC), microscope objective lens (MO), lenses (L1,L2), programmable aperture (PA) and charge-coupled device (CCD). (b) Real space PL, (c) real space masking aperture and (d) corresponding far-field interference pattern of 61 condensates arranged in a triangular geometry.

of the coupled polariton condensate network to gain information about the system's spatial coherence properties. To remove residual PL coming from polaritons outside the condensation (gain)centres we spatially filter the emission of each condensation center and measure the interference of the masked condensate emission in the far field. As schematically illustrated in Figure S2(a) we project the near-field PL onto a programmable aperture which allows to selectively mask the real space field $\Psi(\mathbf{r}, t) \rightarrow A(\mathbf{r})\Psi(\mathbf{r}, t)$ with amplitude function $A(\mathbf{r}) \in (0, 1)$. Subsequently we image the diffraction pattern (far field) onto a charge-coupled device (CCD) sensor. The programmable aperture consists of a digitally controllable reflective liquid-crystal SLM as described in reference [15] and allows to modulate light polarized along the SLM's extraordinary axis. With the use of an additional wave plate and linear polarizer the apparatus transmits only circular polarised light which is chosen to be the same as the polarisation of the pump laser beam. We note that the condensate structures presented in this work are highly polarized with a large degree of circular polarisation conserved from the pump laser. By projecting the near-field PL of the polariton condensate lattice (Figure S2(b)) onto an aperture that transmits only the central FWHM $\approx 2 \mu\text{m}$ of each condensation centre (Figure S2(c)) we record the corresponding far-field emission (Figure S2(d)) that consists of the interference of all condensate nodes. According to the Fraunhofer diffraction formula the measured far-field intensity distribution for a fully coherent wave is proportional to the squared modulus of the Fourier transform of the optical field at the aperture location, which is obtained from Equation (S3) for $|\tilde{\mu}_{ij}| = 1$ for all pairs $\{i, j\}$. Indeed, the appearance of the reciprocal triangular lattice, shown in Figure S2(d), indicates long-range coherence across the triangular lattice of polariton condensates.

5. MEASUREMENT OF COHERENCE IN POLARITON LATTICES

Far field measurements shown in Figure S2 give information about the global coherence properties of the coupled condensate network and are analogous to time-of-flight experiments used in cold atom systems [16]. However, precise information about the local complex coherence factor μ_{ij} can not be obtained. The programmable aperture in our experiment (see Figure S2) overcomes this problem and allows for selective interference between any pair $\{i, j\}$ of condensates, such that the complex coherence factor μ_{ij} can be spatially reconstructed [15, 17]. In particular, the far-field interference of the emission of two spatially filtered condensate nodes $\psi_i(\mathbf{r}, t)$ and $\psi_j(\mathbf{r}, t)$ centred around their respective positions \mathbf{r}_i and \mathbf{r}_j yields the measurable intensity pattern $\tilde{I}_{i+j}(\mathbf{k})$ in \mathbf{k} -space as, [18]

$$\tilde{I}_{i+j}(\mathbf{k}) = \tilde{I}_i(\mathbf{k}) + \tilde{I}_j(\mathbf{k}) + 2\sqrt{\tilde{I}_i(\mathbf{k})\tilde{I}_j(\mathbf{k})} |\tilde{\mu}_{ij}| \cos(\mathbf{k} \cdot \mathbf{d}_{ij} + \tilde{\theta}_{ij}), \quad (\text{S4})$$

where we explicitly take into account non-homogeneous intensity distributions $\tilde{I}_{i,j}(\mathbf{k})$ due to the finite aperture sizes. In Figure S3 we project the triangular lattice of 61 condensates (a) onto three different apertures filtering the emission of the central-most condensate (b), of one of its nearest-neighbours (c) and of both condensates simultaneously (d). The corresponding measured far-field diffraction patterns $\tilde{I}_1(\mathbf{k})$, $\tilde{I}_2(\mathbf{k})$ and $\tilde{I}_{1+2}(\mathbf{k})$ are shown in Figures S3(e-g) respectively. We extract 1D intensity profiles $\tilde{I}(k_{\parallel})$ along the direction vector \mathbf{k}_{\parallel} , which is defined as co-parallel to \mathbf{d}_{12} such that $\mathbf{k}_{\parallel} \cdot \mathbf{d}_{12} = k_{\parallel} |\mathbf{d}_{12}|$. Equation (S4) can be rewritten as,

$$\tilde{I}_{1+2}(k_{\parallel}) = \tilde{I}_1(k_{\parallel}) + \tilde{I}_2(k_{\parallel}) + 2\sqrt{\tilde{I}_1(k_{\parallel})\tilde{I}_2(k_{\parallel})} |\tilde{\mu}_{12}| \cos(k_{\parallel} |\mathbf{d}_{12}| + \tilde{\theta}_{12}), \quad (\text{S5})$$

and is fitted to the experimentally extracted intensity profiles $\tilde{I}_1(k_{\parallel})$, $\tilde{I}_2(k_{\parallel})$ and $\tilde{I}_{1+2}(k_{\parallel})$ to yield $|\tilde{\mu}_{12}|$ and $\tilde{\theta}_{12}$ as shown in Figure S3(h). By extracting $|\tilde{\mu}_{12}|$ for varying pump power we identify the threshold-like behaviour of coherence shown in Figure S3(i) with vanishing coherence between the two nodes below threshold and a sharp increase at threshold. The observed decrease of coherence for larger pump powers $P > 1.2P_{\text{thr}}$ is attributed to effects involving dephasing due to increased particle interactions, reservoir induced noise, enhanced proliferation of topological defects, as well as to the emergence of multi-mode emission [19] reducing the fringe visibility in time-integrated measurements.

Repeating the interference measurement for the central condensate node 1 and each other condensate node j we fully characterise the spatial coherence properties of the central condensate node within the triangular lattice (see Figures S3(j,k) or Figures 1(e,f) in the main text).

6. FINITE VS INFINITE LATTICE

In experiment finite-size effects cannot be avoided whereas in theory they can be avoided by applying periodic boundary conditions. In Figure S4 we investigate the difference of finite and periodic systems through simulation of Equation (S1). In agreement with experiment, and previous theoretical observations [12], the pseudo-spin of $\tilde{\mu}_{ij}$ tilts as one approaches the edges of the finite (damped

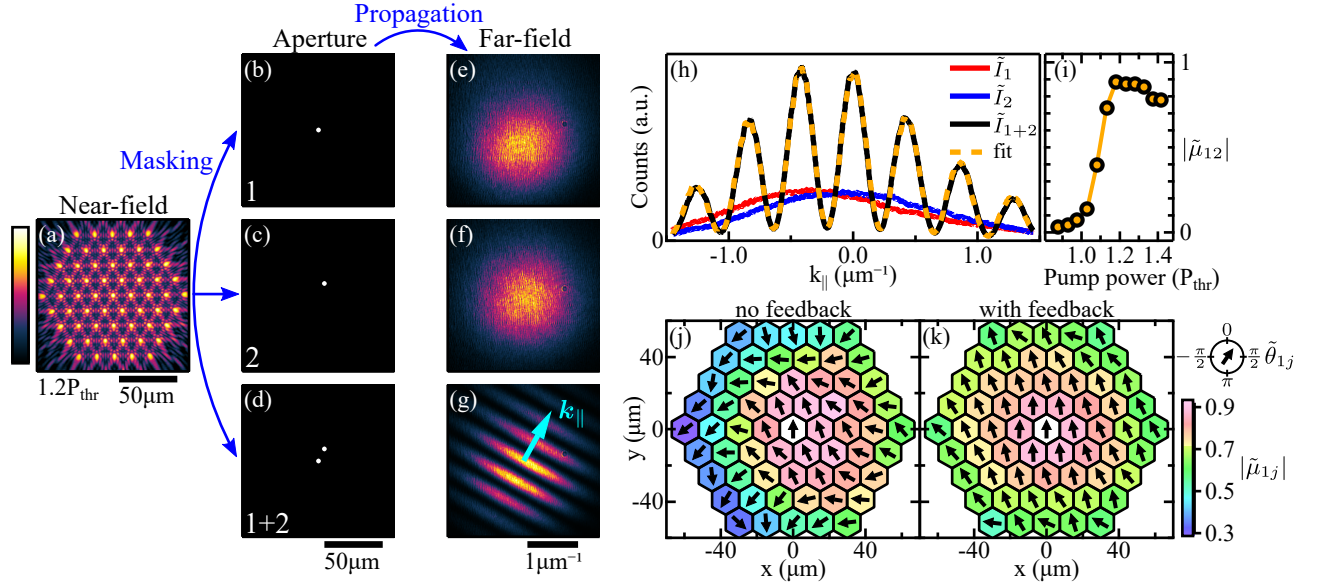


Fig. S3. Measurement of spatial coherence in lattices of coupled polariton condensates. By projecting the (a) real space PL of a lattice of coupled condensates onto a programmable aperture that spatially filters the emission to transmit only (b) condensate node 1, (c) condensate node 2 or (d) both condensate nodes 1 + 2 we record the respective far-field emission (e-g). The extracted intensity profiles $\tilde{I}_1(k_{\parallel})$, $\tilde{I}_2(k_{\parallel})$ and $\tilde{I}_{1+2}(k_{\parallel})$ perpendicular to the orientation of the interference fringes in (g) are shown in (h) together with a fit according to Equation (S5). Pump power-dependence of the modulus of the integrated coherence factor $|\tilde{\mu}_{12}|$ is displayed in (i). Extracted values of the integrated complex coherence factor $\tilde{\mu}_{1i}$ between the central condensate node 1 and each other condensate node i are illustrated in (j) and (k) for the cases of no condensate node density stabilisation and with node density stabilisation. All values are extracted at a total pump power $P = 1.2P_{\text{thr}}$. False colour scale shown for (a) applies to (e-g) in linear scale and to (a) in logarithmic scale saturated below 0.01 of the maximum count rate.

boundary condition) condensate lattice (see Figure S4(c)). This effect is expected due to the non-zero flux of particles through the boundaries of the lattice resulting in a phase gradient differing from standing wave solutions of $\tilde{\theta}_{ij} = 0, \pi$. When the system has periodic boundary conditions (see Figure S4(d)) the pseudo-spin tilt vanishes and the lattice is characterised by a homogeneous standing wave solution (zero net-flux along x and y directions). The simulation in both cases uses a lattice constant of $a = 12 \mu\text{m}$ and is performed on a $16a \times 16a$ grid but we only plot the innermost $11a \times 11a$ of the grid. Therefore, removing finite size effects results in a homogeneous power distribution among all condensate nodes and thus the phases-differences stay homogeneously 0 or π .

We point out that by simulating a periodic system the coherence has dropped by a small amount. This can be understood from the fact that each pulse proliferates vortex solitons [20] which, in a finite system, can decay out through the boundary of the system (i.e., damped boundary conditions destroy such defects). In the absence of such a decay channel, these defect states can survive much longer in a periodic system leading to a drop in coherence.

7. EXCITATION PUMP POWER DEPENDENCE

In this section we describe the pump power dependence of the stabilised triangular lattice of 61 ballistically coupled polariton condensates with lattice constant $a = 14.9 \mu\text{m}$ shown in Figures 1 and 2 in the main text. For the case of pulsed excitation the pump power P is a time-averaged value and a change of P is equivalent

to changing the peak amplitude of the sub-picosecond laser pulse. The recorded emission patterns for pump power $P = 1.2P_{\text{thr}}$ in near-field, far-field and energy resolved far-far-field along the symmetry axis $k_x = 0$ are illustrated in Figures S5(a,c,e). The pump power geometry was adjusted using the described iterative feedback algorithm to stabilise the emission power of all condensates at threshold such that the spread of measured condensate emission powers shows a minimum of 1% (RSD) for $P = P_{\text{thr}}$. In Figure S5(b) we show the spread of condensate emission powers for varying total excitation pump power while keeping the relative pump power between different nodes constant. An increase of the spread above condensation threshold to about 20% at $P = 1.2P_{\text{thr}}$ originates from the different number of coupled neighbouring sites between condensates in the centre and at the edge of the lattice structure leading to different additional gain from coherent coupling between condensate nodes.

In Figure S5(d) we illustrate the pump power dependence of the total integrated PL demonstrating a threshold level with non-linear increase of PL intensity which we define as condensation threshold P_{thr} . An increase in pump power from condensation threshold P_{thr} to the operational point $P = 1.2P_{\text{thr}}$ leads to a 9-fold increase of total PL power.

The spectrally resolved PL in reciprocal space along the symmetry axis $k_x = 0$ in Figure S5(e) demonstrates PL emission at one dominant mode with FWHM $\approx 250 \mu\text{eV}$. In agreement with the threshold-like behaviour of the integrated PL we can see a sharp narrowing of polariton linewidth at condensation threshold which is shown in Figure S5(f).

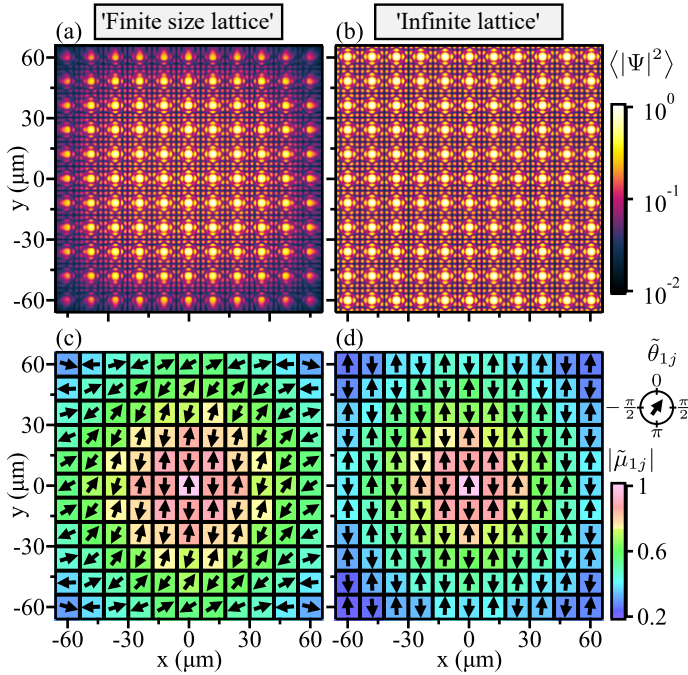


Fig. S4. Numerical simulation of a square lattice of ballistically expanding polariton condensates with damped (a,c) and periodic boundary conditions (b,d). (a,b) Time-integrated and normalised real space densities for both types of lattices with equal pump power for each condensate node. (c,d) Extracted absolute values and phases of the complex degree of coherence μ_{1j} between the most central condensate node (index 1, located at $x, y = 0$) and every other condensate node (index j). The lattice constant is $a = 12 \mu\text{m}$ and size of simulation grid is $16a \times 16a$ with displayed results are zoomed in on an area of $11a \times 11a$.

8. TIME-RESOLVED SYNCHRONISATION OF TWO CONDENSATES

The time-resolved formation of coherence in polariton condensates under non-resonant pulsed excitation has been investigated for single- [21–23] and two-condensate systems [19, 24]. In the latter case, however, a full description of the synchronisation process between two condensates in terms of their complex coherence factor has not been reported. Here, we explicitly measure the (time-resolved) complex coherence factor $\mu_{12}(t)$ of two ballistically coupled condensation centres. Pulsed excitation of two condensates with separation distance $d_{12} = 8 \mu\text{m}$ leads to the time-averaged near-field photoluminescence displayed in Figure S6(a). The pump power $P \approx 1.2P_{\text{thr}}$ is the same as for the distance-dependence shown in Figure 3 in the main text. One bright interference peak located in-between the two condensation centres at $x, y = 0$ indicates synchronisation with vanishing phase-difference, i.e. $\theta_{12} = 0$. To reveal the coherence properties between the two condensates we record their far-field interference by spatially filtering the emission of both condensation centres (red-dashed circles) as shown in Figure S6(b). The modulus of the integrated coherence factor from this time-averaged interference pattern is extracted as $|\tilde{\mu}_{12}| = 0.94$. By projecting the far-field pattern onto the entrance slit of a streak camera (time resolution

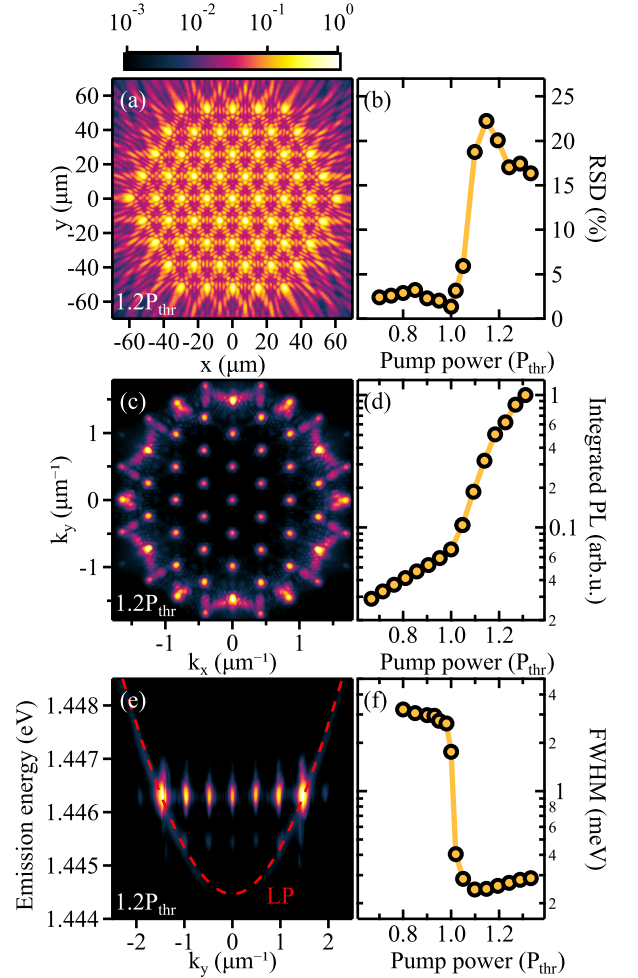


Fig. S5. Pump-power dependence of a triangular lattice of polariton condensates. (a) Recorded near-field photoluminescence of 61 polariton condensates pumped at 1.2 times condensation threshold. (b) Pump-power dependence of the relative standard deviation (RSD) of the distribution of integrated condensate emission. The system was stabilised to obtain minimum RSD (1%) at condensation threshold P_{thr} . (c) Recorded far-field photoluminescence for $P = 1.2P_{\text{thr}}$. (d) Pump-power dependence of the integrated emission in reciprocal space. (e) Spectrally-resolved momentum space emission along the symmetry axis $k_x = 0$ for $P = 1.2P_{\text{thr}}$. Lower polariton branch below threshold shown as red-dashed dispersion curve. (f) Pump-power dependence of the spectral full width at half maximum.

$\Delta t \approx 2 \text{ ps}$) we resolve the interference and emission of each individual condensate node in time as shown in Figures S6(c-e). We extract the time-dynamics of the mutual complex degree of coherence $\mu_{12}(t)$ from the measured interference and reference signals and illustrate its phase $\theta_{12}(t)$ and modulus $|\mu_{12}(t)|$ in Figures S6(f) and (g), respectively. The time-resolved occupation $\Gamma_{11}(t) + \Gamma_{22}(t)$ with $\Gamma_{ii}(t) = \langle |\psi_i(t)|^2 \rangle$ of both condensates is shown in Figure S6(h) and reveals pulsed polariton emission with temporal width $\approx 18 \text{ ps}$ (FWHM) and peak signal at 50 ps after excitation with the pump laser. We find complete synchronisation

with $\theta_{12} = 0$ and a maximum degree of coherence $|\mu_{12}| = 1$ appearing earlier than the peak PL signal at $t = 41$ ps still during the condensate growth time. The subsequent temporal decay of mutual coherence is slower than the decay of total condensate population with fitted $1/e$ decay times of 80 ps and 13 ps, respectively. We note that different growth and decay dynamics between population and coherence in single-condensate systems have been reported in Ref. [21] and Ref. [22].

9. COMPARISON TO CONTINUOUS WAVE EXCITATION

We compare the results of mutual coherence between two ballistically expanding polariton condensates pumped under sub-picosecond excitation shown in Figure 3 in the main text to the case of pumping using continuous wave (cw) monomode laser excitation. To prevent heating of the microcavity sample under cw excitation, the excitation laser is modulated by an acousto-optic modulator to generate square wave packets of 5 μs duration at a frequency of 10 kHz. In Figures S7(a) and (b) we illustrate the recorded near-field and far-field photoluminescence of two condensate with separation distance $d = 12$ μm . The system is pumped at $P = 1.6P_{\text{thr}}$ with a threshold pump power $P_{\text{thr}} \approx 10$ mW per condensate node as shown in Figure S7(c). We note that the near-field and far-field excitation pattern in Figures S7(a) and (b) are different to the emission patterns shown in Figures 3(a) and (b) in the main text under pulsed excitation despite a small difference in pump spot separation distance of less than 1 μm . In both cases the emission patterns indicate synchronisation in a state with π phase-difference between the two condensate nodes. However, the outflow wavevector (or alternatively in-plane momentum) of polaritons under pulsed excitation is larger than under cw excitation leading to a smaller interference fringe periodicity in both real- and momentum-space.

The extracted decay of the complex coherence factor μ_{12} with increasing condensate separation distance under cw excitation is illustrated in Figure S7(d). In the same plot we show the dependency of the integrated complex coherence factor $\tilde{\mu}_{12}$ on the separation distance d_{12} of two condensates under pulsed excitation (as presented in Figure 3 in the main text). While both systems demonstrate similar coherence properties for condensate separation distances $d_{12} \leq 20$ μm , the stationary system's coherence $|\mu_{12}|$ is enhanced for distances larger than 20 μm as compared to the nonstationary system under sub-picosecond pulsed excitation. A Gaussian fit (see Equation 2 in the main text) of the decay of coherence $|\mu_{12}(d_{12})|$ with increasing condensate spacing under cw excitation yields an effective coherence length $L_C = 40$ μm . We argue that the build-up of coherence $|\mu_{12}(t)|$ between the two ballistically coupled condensates under pulsed excitation (as described in Supplementary Section 8) is fast enough for small distances $d_{12} \leq 20$ μm as to synchronise and reach the same coherence $|\mu_{12}|$ as in steady-state operation. For larger distances, however, the increased time-of-flight of particles travelling in-between the two condensate nodes [25] becomes noticeable and reduces the coherence factor $|\tilde{\mu}_{12}|$ of the nonstationary system with finite life-time.

10. BOGOLIUBOV ANALYSIS

Let us consider the continuous-wave excitation regime where $n_c(\mathbf{r}) = P(\mathbf{r})$ is taken time-independent. We will also consider the

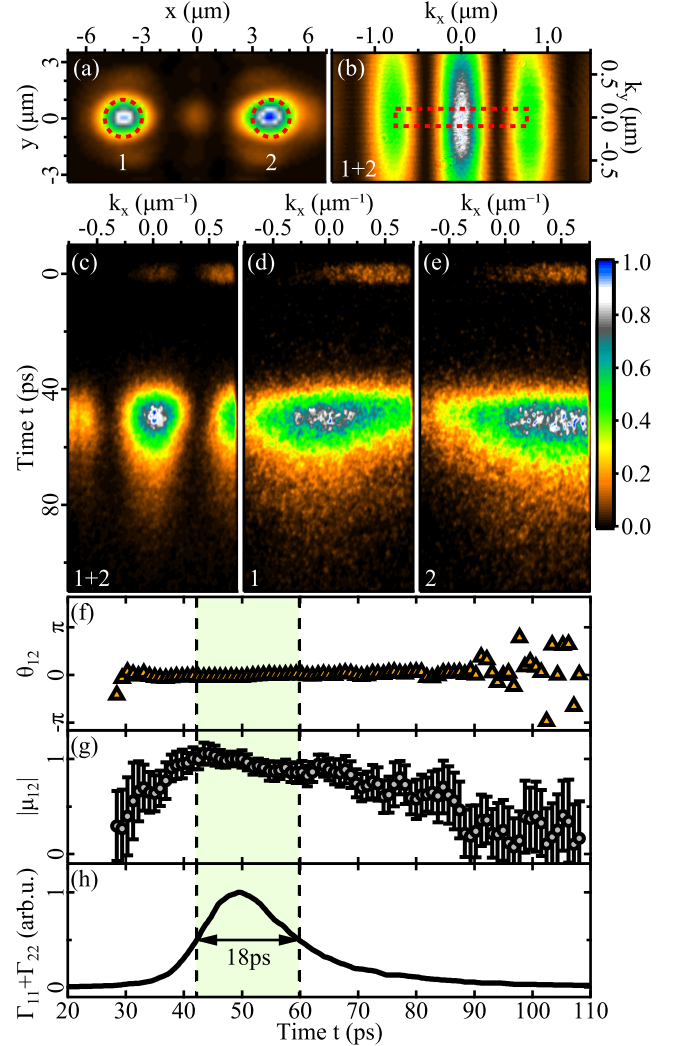


Fig. S6. Synchronisation of two ballistically coupled polariton condensates. (a) Near-field photoluminescence of two condensates with separation distance $d_{12} = 8$ μm . (b) Recorded far-field photoluminescence when filtering the emission of the condensate centres marked with red dashed circles in (a). (c-e) Time-resolved and normalised far-field photoluminescence for both condensates interfering (1 + 2) and individually (1, 2) recorded by projecting the photoluminescence onto the entrance slit of a streak camera (red-dashed rectangle in (b)). Time-dependencies of extracted phase difference θ_{12} , the modulus of the complex degree of coherence $|\mu_{12}|$ and the total emission signal $\Gamma_{11} + \Gamma_{22}$ of both condensate nodes are shown in (f-h). The emission signal $\Gamma_{11} + \Gamma_{22}$ is extracted by spatial integration of the signals in (d) and (e). The origin for the time axis in (f-h) is defined by the laser arrival time. The full width at half maximum of the emission signal (≈ 18 ps) is highlighted in light green.

ideal case of no stochasticity by setting $dW = 0$. Assuming that the reservoir n_x follows the dynamics of the condensate we can perform an adiabatic elimination of Equation (S1b) and keeping

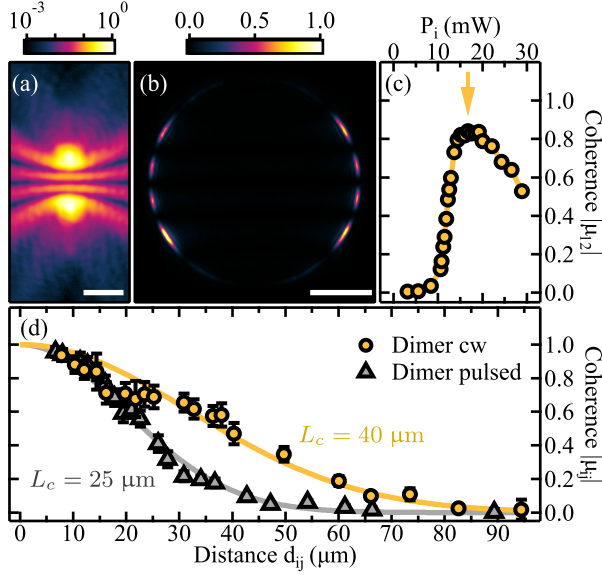


Fig. S7. Ballistic coupling of two polariton condensates pumped under continuous wave (cw) excitation. Recorded (a) near-field and (b) far-field photoluminescence for two condensates separated by $d_{12} = 12 \mu\text{m}$. (c) Extracted mutual coherence factor $|\mu_{12}|$ between the two condensates as a function of excitation pump power P_i per condensate. Vertical arrow marks the fixed pump power ($P \approx 1.6P_{\text{thr}}$) for data shown in (a,b) and for the condensate separation distance dependence shown in (d). The data points of a dyad under pulsed excitation (grey triangles) are illustrated for comparison to the system under cw excitation (orange circles). Curves in (d) represent Gaussian fits. Scale bars in (a) and (b) correspond to $10 \mu\text{m}$ and $1 \mu\text{m}^{-1}$, respectively.

terms to the first order in R in Equation (S1a) we have,

$$i \frac{\partial \Psi}{\partial t} = \left[-\frac{\hbar \nabla^2}{2m} + gP(\mathbf{r}) + \alpha |\Psi|^2 + \frac{iP}{2} \left(1 - \frac{|\Psi|^2}{n_s} \right) - \frac{i\gamma}{2} \right] \Psi, \quad (\text{S6})$$

where $n_s = \Gamma_R/R$. Performing the standard Bogoliubov treatment where the condensate wavefunction Ψ is expanded around a fixed point solution Ψ_0 of Equation (S6) with energy $\hbar\nu$ we write,

$$\Psi = \Psi_0(\mathbf{r}) e^{-i\nu t} \left[1 + \sum_{\mathbf{q}} \left(u_{n,\mathbf{q}} e^{i\mathbf{q}\cdot\mathbf{r} + \lambda_n t} + v_{n,\mathbf{q}} e^{-i\mathbf{q}\cdot\mathbf{r} + \lambda_n^* t} \right) \right] \quad (\text{S7})$$

We wish to scrutinise the dispersion of elementary excitations (Lyapunov exponents) with complex energies λ_n . We point out that the connection between the Lyapunov exponents and Bogoliubov elementary excitations ω_n [26] is simply $\lambda_n = -i\omega_n$ seen from Eq. Eq. (S7). Substitution of Equation (S7) into Equation (S6) and keeping only terms linear in $u_{n,\mathbf{q}}$ and $v_{n,\mathbf{q}}$ we obtain a linearised set of equations of motion for the disturbances. We assume that the potential V and condensate Ψ_0 are infinite and periodic such that $P(\mathbf{r}) = P(\mathbf{r} + \mathbf{a})$ and $|\Psi_0(\mathbf{r})|^2 = |\Psi_0(\mathbf{r} + \mathbf{a})|^2$, where $\mathbf{a} = n_1 \mathbf{a}_1 + n_2 \mathbf{a}_2$ is the translational symmetry vector defined in the bases of primitive lattice vectors $\mathbf{a}_{1,2}$ for some integers $n_{1,2}$. We can then apply Bloch's theorem where we write the disturbances wavefunction in the factorised form of crystal momentum

$\mathbf{q} = (q_x, q_y)$ and Bloch states in the n th band $u_{n,\mathbf{q}}(\mathbf{r}) = u_{n,\mathbf{q}}(\mathbf{r} + \mathbf{a})$ and $v_{n,\mathbf{q}}(\mathbf{r}) = v_{n,\mathbf{q}}(\mathbf{r} + \mathbf{a})$.

$$\mathbf{B}_{n,\mathbf{q}}(\mathbf{r}) = \begin{pmatrix} u_{n,\mathbf{q}}(\mathbf{r}) \\ v_{n,\mathbf{q}}(\mathbf{r}) \end{pmatrix}. \quad (\text{S8})$$

By Fourier transforming periodic terms into the basis of reciprocal lattice vectors we can easily solve the energies λ_n belonging to $u_{n,\mathbf{q}}$ and $v_{n,\mathbf{q}}$,

$$\mathcal{L}(\mathbf{q}, \Psi_0) \mathbf{B}_{n,\mathbf{q}} = \lambda_n(\mathbf{q}) \mathbf{B}_{n,\mathbf{q}}, \quad (\text{S9})$$

where \mathcal{L} is our Bogoliubov (Lyapunov) matrix in the crystal momentum representation,

$$\begin{aligned} \mathcal{L}(\mathbf{q}, \Psi_0) = & \frac{\hbar}{2m} \left[\left(q_x - i \frac{\partial}{\partial x} \right)^2 + \left(q_y - i \frac{\partial}{\partial y} \right)^2 \right] \hat{\sigma}_3 \\ & + \left[gP(\mathbf{r}) - \nu + 2\alpha |\Psi_0|^2 \right] \hat{\sigma}_3 + \frac{i}{2} \left(P - \gamma - 2P \frac{|\Psi_0|^2}{n_s} \right) \hat{\sigma}_0 \\ & + \alpha \begin{pmatrix} 0 & \Psi_0^2 \\ -(\Psi_0^*)^2 & 0 \end{pmatrix} - \frac{iP}{2n_s} \begin{pmatrix} 0 & \Psi_0^2 \\ (\Psi_0^*)^2 & 0 \end{pmatrix}. \end{aligned} \quad (\text{S10})$$

The solution Ψ_0 satisfying Equation (S6) can be obtained numerically using periodic boundary conditions. Plugging the obtained solution Ψ_0 , which corresponds to observed condensate patterns in experiment, into the eigenvalue problem for $\mathbf{B}_{n,\mathbf{q}}$ we can finally diagonalise our system.

11. FAR-FIELD DIFFRACTION FOR NARROW-BANDWIDTH PARTIALLY COHERENT LIGHT

Let us assume the narrow bandwidth optical field $\Psi(\mathbf{r}, t) = \psi(\mathbf{r}, t) \exp(-i2\pi ct/\bar{\lambda})$ with mean wavelength $\bar{\lambda}$ is being truncated by a thin aperture with transmittance function $P(\mathbf{r})$ in the plane \mathcal{A} such that the field directly after the aperture is given by the product $P(\mathbf{r})\Psi(\mathbf{r}, t)$. The signal's bandwidth $\Delta\nu$ is assumed to be much smaller than the central frequency $\bar{\nu} = c/\bar{\lambda}$ such that the complex amplitude $\psi(\mathbf{r}, t)$ is a slowly varying envelope in time. The average intensity distribution $\bar{I}(\mathbf{q})$ of the resulting far-field diffraction pattern described in coordinate basis \mathbf{q} - realised at the back focal plane of a thin Fourier-transforming lens with focal length f - in analogy to Schell's theorem [27] can be approximated as

$$\bar{I}(\mathbf{q}) = \iint_{\mathcal{A}} \iint_{\mathcal{A}} P^*(\mathbf{r}_1) P(\mathbf{r}_2) \sqrt{\bar{I}(\mathbf{r}_1) \bar{I}(\mathbf{r}_2)} \tilde{\mu}(\mathbf{r}_1, \mathbf{r}_2) \frac{e^{i\frac{2\pi}{\bar{\lambda}} \mathbf{q} \cdot \mathbf{d}_{12}}}{(\bar{\lambda}f)^2} d\mathbf{r}_1 d\mathbf{r}_2, \quad (\text{S11})$$

with distance vector $\mathbf{d}_{12} = \mathbf{r}_1 - \mathbf{r}_2$, integrated complex coherence factor $\tilde{\mu}(\mathbf{r}_1, \mathbf{r}_2)$ and average intensity $\bar{I}(\mathbf{r}_{1,2})$ of the optical field $\psi(\mathbf{r}_{1,2}, t)$ at locations $\mathbf{r}_{1,2}$ in the input plane \mathcal{A} . We further approximate a distribution of point-like holes in the aperture, i.e.

$$P(\mathbf{r}) = A_0 \sum_i \delta(\mathbf{r} - \mathbf{r}_i), \quad (\text{S12})$$

where A_0 corresponds to the finite physical size of each hole, and we transform into the basis of spatial frequencies $\mathbf{k}(\mathbf{q}) = 2\pi\mathbf{q}/\bar{\lambda}f$ yielding

$$\bar{I}(\mathbf{k}) = \frac{A_0^2}{(\bar{\lambda}f)^2} \sum_{ij} \sqrt{\bar{I}(\mathbf{r}_i) \bar{I}(\mathbf{r}_j)} \tilde{\mu}(\mathbf{r}_i, \mathbf{r}_j) e^{i\mathbf{k} \cdot \mathbf{d}_{ij}}. \quad (\text{S13})$$

Under the assumption of a fully coherent field with constant coherence factor $\tilde{\mu}(\mathbf{r}_i, \mathbf{r}_j) = 1$ the resultant far-field diffraction pattern (Equation (S13)) reduces to the well-known Fraunhofer diffraction formula,

$$\tilde{I}(\mathbf{k}) = \left| \frac{A_0}{\lambda f} \sum_i \sqrt{\tilde{I}(\mathbf{r}_i)} e^{i\mathbf{k} \cdot \mathbf{r}_i} \right|^2. \quad (\text{S14})$$

It is apparent from Equation (S14) that in case of a periodic arrangement (lattice) of aperture holes at locations \mathbf{r}_i the resultant intensity distribution $\tilde{I}(\mathbf{k})$ is formed by the squared modulus of the discrete Fourier-transform of the optical field sampled at locations \mathbf{r}_i .

REFERENCES

1. P. Cilibrizzi, A. Askitopoulos, M. Silva, F. Bastiman, E. Clarke, J. M. Zajac, W. Langbein, and P. G. Lagoudakis, "Polariton condensation in a strain-compensated planar microcavity with InGaAs quantum wells," *Appl. Phys. Lett.* **105**, 191118 (2014).
2. M. Wouters and V. Savona, "Stochastic classical field model for polariton condensates," *Phys. Rev. B* **79**, 165302 (2009).
3. T. Gao, C. Antón, T. C. H. Liew, M. D. Martín, Z. Hatzopoulos, L. Viña, P. S. Eldridge, and P. G. Savvidis, "Spin selective filtering of polariton condensate flow," *Appl. Phys. Lett.* **107**, 011106 (2015).
4. R. Gerchberg and W. Saxton, "A practical algorithm for the determination of phase from image and diffraction plane pictures," *Optik* **35**, 237–246 (1972).
5. F. Nogrette, H. Labuhn, S. Ravets, D. Barredo, L. Béguin, A. Vernier, T. Lahaye, and A. Browaeys, "Single-atom trapping in holographic 2d arrays of microtraps with arbitrary geometries," *Phys. Rev. X* **4**, 021034 (2014).
6. H. Tamura, T. Unakami, J. He, Y. Miyamoto, and K. Nakagawa, "Highly uniform holographic microtrap arrays for single atom trapping using a feedback optimization of in-trap fluorescence measurements," *Opt. express* **24**, 8132–8141 (2016).
7. M. Wouters and I. Carusotto, "Excitations in a nonequilibrium Bose-Einstein condensate of exciton polaritons," *Phys. Rev. Lett.* **99**, 140402 (2007).
8. N. Bobrovska, E. A. Ostrovskaya, and M. Matuszewski, "Stability and spatial coherence of nonresonantly pumped exciton-polariton condensates," *Phys. Rev. B* **90**, 205304 (2014).
9. F. Baboux, D. D. Bernardis, V. Goblot, V. N. Gladilin, C. Gomez, E. Galopin, L. L. Gratiet, A. Lemaître, I. Sagnes, I. Carusotto, M. Wouters, A. Amo, and J. Bloch, "Unstable and stable regimes of polariton condensation," *Optica* **5**, 1163–1170 (2018).
10. E. Wertz, L. Ferrier, D. D. Solnyshkov, R. Johne, D. Sanvitto, A. Lemaître, I. Sagnes, R. Grousson, A. V. Kavokin, P. Senellart, G. Malpuech, and J. Bloch, "Spontaneous formation and optical manipulation of extended polariton condensates," *Nat. Phys.* **6**, 860–864 (2010).
11. P. Cristofolini, A. Dreismann, G. Christmann, G. Franchetti, N. G. Berloff, P. Tsotsis, Z. Hatzopoulos, P. G. Savvidis, and J. J. Baumberg, "Optical superfluid phase transitions and trapping of polariton condensates," *Phys. Rev. Lett.* **110**, 186403 (2013).
12. K. P. Kalinin and N. G. Berloff, "Networks of non-equilibrium condensates for global optimization," *New J. Phys.* **20**, 113023 (2018).
13. E. A. Ostrovskaya, J. Abdullaev, M. D. Fraser, A. S. Desyatnikov, and Y. S. Kivshar, "Self-localization of polariton condensates in periodic potentials," *Phys. Rev. Lett.* **110**, 170407 (2013).
14. S. Mahler, M. L. Goh, C. Tradonsky, A. A. Friesem, and N. Davidson, "Improved phase locking of laser arrays with nonlinear coupling," *Phys. Rev. Lett.* **124**, 133901 (2020).
15. G. P. Lousberg, L. D. Lundberg, D. L. Boiko, and E. Kapon, "Space-domain lock-in amplifier based on a liquid-crystal spatial light modulator," *Opt. Lett.* **31**, 990–992 (2006).
16. Z. Hadzibabic, P. Krüger, M. Cheneau, B. Battelier, and J. Dalibard, "Berezinskii-Kosterlitz-Thouless crossover in a trapped atomic gas," *Nature* **441**, 1118–1121 (2006).
17. L. D. A. Lundberg, G. P. Lousberg, D. L. Boiko, and E. Kapon, "Spatial coherence measurements in arrays of coupled vertical cavity surface emitting lasers," *Appl. Phys. Lett.* **90**, 021103 (2007).
18. B. J. Thompson and E. Wolf, "Two-beam interference with partially coherent light," *J. Opt. Soc. Am.* **47**, 895–902 (1957).
19. H. Ohadi, R. L. Gregory, T. Freearde, Y. G. Rubo, A. V. Kavokin, N. G. Berloff, and P. G. Lagoudakis, "Nontrivial phase coupling in polariton multiplets," *Phys. Rev. X* **6**, 031032 (2016).
20. D. N. Neshev, T. J. Alexander, E. A. Ostrovskaya, Y. S. Kivshar, H. Martin, I. Makasyuk, and Z. Chen, "Observation of discrete vortex solitons in optically induced photonic lattices," *Phys. Rev. Lett.* **92**, 123903 (2004).
21. E. del Valle, D. Sanvitto, A. Amo, F. P. Laussy, R. André, C. Tejedor, and L. Viña, "Dynamics of the formation and decay of coherence in a polariton condensate," *Phys. Rev. Lett.* **103**, 096404 (2009).
22. G. Nardin, K. G. Lagoudakis, M. Wouters, M. Richard, A. Baas, R. André, L. S. Dang, B. Pietka, and B. Deveaud-Plédran, "Dynamics of long-range ordering in an exciton-polariton condensate," *Phys. Rev. Lett.* **103**, 256402 (2009).
23. V. V. Belykh, N. N. Sibeldin, V. D. Kulakovskii, M. M. Glazov, M. A. Semina, C. Schneider, S. Höfling, M. Kamp, and A. Forchel, "Coherence expansion and polariton condensate formation in a semiconductor microcavity," *Phys. Rev. Lett.* **110**, 137402 (2013).
24. G. Christmann, G. Tosi, N. G. Berloff, P. Tsotsis, P. S. Eldridge, Z. Hatzopoulos, P. G. Savvidis, and J. J. Baumberg, "Oscillatory solitons and time-resolved phase locking of two polariton condensates," *New J. Phys.* **16**, 103039 (2014).
25. J. Töpfer, H. Sigurdsson, L. Pickup, and P. Lagoudakis, "Time-delay polaritonics," *Commun. Phys.* **3**, 1–8 (2020).
26. L. Pitaevskii and S. Stringari, *Bose-Einstein condensation and superfluidity*, vol. 164 (Oxford University Press, 2016).
27. J. W. Goodman, *Statistical optics* (John Wiley & Sons, 2015).